J. Astrophys. Astr. (2025) 46:77
https://doi.org/10.1007/s12036-025-10104-5
© Indian Academy of Sciences

A kinematic and structural study of young open clusters in the Milky Way galaxy using *Gaia* DR3 catalogue

K. H. HARSHA[1,2,*], ANNAPURNI SUBRAMANIAM[2], S. R. DHANUSH[2,3] and D. S. HARIHARAN[4]

[1]Indian Institute of Science Education and Research, Tirupati 517619, India.
[2]Indian Institute of Astrophysics, 2nd Block Koramangala, Bangalore 560034, India.
[3]Pondicherry University, R.V. Nagar, Kalapet, Puducherry 605014, India.
[4]Center for Astrophysics Research (CAR), University of Hertfordshire, Hatfield, UK.
*Corresponding author. E-mail: harshakh99@gmail.com

MS received 14 April 2025; accepted 24 July 2025

Abstract. We aim to identify the cluster members, estimate cluster properties, study the dynamical state of the clusters as a function of mass, trace the existence of dynamical effects in massive stars, and check for spatial patterns of members in young clusters. We studied 14 young open clusters located within 1 kpc using the data from *Gaia* DR3 with the membership estimated using the GMM method. The cluster parameters, such as age, distance, metallicity, and extinction were estimated by fitting PARSEC isochrones to the CMDs. These clusters are found to have ages between 6 and 90 Myr, located between 334 and 910 pc, covering a mass range of 0.13–13.77 $M_{\odot}$. In five of these clusters, stars from F to M spectral type show increasing velocity dispersion, a signature for dynamical relaxation. We detect high proper motion for B and A-type stars, possible walkaway stars in the other five clusters, Alessi Teutsch 5, ASCC 16, ASCC 21, IC 2395, and NGC 6405. We demonstrate the existence of mass-dependent velocity dispersion in young clusters, suggestive of dynamical relaxation. The typical range of transverse velocity dispersion is found to be 0.40–0.70 km s^{-1} for young clusters.

Keywords. Open clusters—isochrone fitting—transverse velocity dispersion.

1. Introduction

Stars form in molecular clouds, mostly in groups or clusters (Lada & Lada 2003). Star clusters have always served as an open laboratory for various stellar evolutionary studies (Cantat-Gaudin *et al.* 2020). As star clusters are the fundamental building blocks of our Galaxy (Kharchenko *et al.* 2013), studying them can help us understand the evolution and structure of the galaxies that comprise the universe (Cantat-Gaudin *et al.* 2020).

Star clusters comprising population I stars in our galaxy are known as open clusters (OCs). These are loosely bound by gravitation and go through various dynamical processes, such as tidal perturbation due to the galactic disk, internal interaction between members, and feedback from stellar evolution leading to the evaporation in 100 Myr (Wielen 1971). Park *et al.* (2017), suggested from their numerical simulation that star clusters are rapidly destroyed in the inner galactic disk, where there is a strong effect of the tidal field. Bergond *et al.* (2001) have explained the effect of time-varying tidal fields during disc shocks in the dynamical evolution of OCs. From their simulation, they suggested that about 20% of mass is lost during this process, and the destruction time scale is around 600 Myr for the OCs. One of the major assumptions in the simulation is the internal velocity dispersion in OCs as well as the dynamical state of the cluster members. It is therefore important to derive the observed spatial and kinematical properties of young surviving open clusters to provide realistic parameters for simulations.

The clusters go through dynamical relaxation over a time scale, leading to the segregation of massive stars towards the center and energy equipartition. The relaxation may lead to more massive stars having closer orbits and less massive stars with extended orbits with respect to the center of the cluster (Sagar & Bhatt 1989).

Published online: 14 October 2025

Lada *et al.* (1984) and Margulis & Lada (1984) studied the dynamical evolution of young open clusters with about 100 members and found that, as a result of two-body interactions, mass segregation may occur after 2–3 Myr. This study suggested that less massive stars relax relatively quickly, leading to mass segregation. The presence of mass segregation or dynamical relaxation can be traced by detecting mass-dependent velocity dispersion in young clusters. This was attempted long back by Sagar & Bhatt (1989).

Earlier, McNamara & Sekiguchi (1986) studied the internal kinematics of M35 OC, suggesting that the velocity-mass relation may not be satisfied by high-mass stars (1.2–5.6 $M_{\odot}$). Later, Sagar & Bhatt (1989) agreed with this study from their findings that the equipartition of energy may not be valid for all the clusters. They also suggested that the velocity-mass relation can be affected by the galactic field, dynamical evolution, and initial star-forming conditions. Recently, Bhattacharya *et al.* (2022) studied the tidal tails and mass segregation in OCs using *Gaia* EDR3. They found that mass segregation is mostly observed in older OCs.

Some of the high-mass stars, runaway stars, in the clusters have unusually high velocity, and most of such are seen in the dense and low-mass clusters (Fujii & Portegies Zwart 2011). The term 'runaway stars' was first coined by Blaauw (1961) to represent high-mass stars that have unusually high velocity (>30 km s^{-1}). This high velocity can be due to dynamical ejection or binary interactions (Poveda *et al.* 1967; Leonard 1991; Allen & Kinman 2004). Massive stars play a key role in enriching the interstellar medium (ISM); therefore, runaway stars contribute to enriching the regions of the ISM far away from their birthplace. There could be many unbound massive stars that are slower and hence not included in the runaway stars. Many suggested there can be unbound massive stars with velocity <30 km s^{-1} (Eldridge *et al.* 2011; de Mink *et al.* 2012; Perets & Šubr 2012; Renzo *et al.* 2019) and such stars are termed 'walkaway stars' (de Mink *et al.* 2012). With the availability of large data with precise kinematic information, studies are growing to identify such stars and their origin.

There are four main objectives for this study. Firstly, to identify the cluster members and precise cluster properties, which can be used as probes to explore star formation and dynamics. Next, we will study the dynamical state of the young clusters as a function of mass using transverse velocity dispersion. Then, to trace the existence of dynamical effects in massive stars and the existence of unbound stars, such as walkaway stars. Finally, to trace the imprints and patterns of star formation in OCs. Now, with the availability of more precise and accurate astrometric and photometric data from *Gaia* DR3, it is possible to derive highly reliable membership information and cluster parameters that are vital to derive the dynamical state of OCs. In this work, we studied the kinematic and structural properties of 14 OCs. We selected the target OCs by filtering the clusters that are less than 100 Myr of age and within 1 kpc distance from the Cantat-Gaudin catalog (Cantat-Gaudin *et al.* 2020). Choosing OCs within 1 kpc allows us to reduce errors in parameter estimation and to detect low-mass members.

The paper is arranged as follows: In Section 2, we describe the data and methods used for the purpose of analysis. In Section 3, we present the results obtained from the analysis and discuss our main findings. Finally, we conclude our paper with Section 4.

2. Data, methods, and analysis

Gaia mission surveys a large area of space (including the Milky Way galaxy and a significant amount of extra-galactic objects) and collects astrometric, photometric, and spectrometric data with high precision for over 1.8 billion stars (Gaia Collaboration *et al.* 2023). A total of 4 data releases, DR1, DR2, EDR3, and DR3, have been released, with the recent data release (*Gaia* DR3) having high precision proper motion (PM) values Gaia Collaboration *et al.* (2023). The *Gaia* DR3 data for 14 clusters were downloaded from the *Gaia* archive with a radius of r50×2 from its central coordinate, where r50 is the radius containing half of the cluster members, obtained from Cantat-Gaudin *et al.* (2020), Table A1. In the case of Alessi Teutsch 5, we have opted for a radius smaller than that mentioned in Cantat-Gaudin *et al.* (2020) due to the presence of another cluster closer to it. The cluster parameters required for the analysis were also taken from Cantat-Gaudin *et al.* (2020).

2.1 *Data filtering*

We needed to remove the obvious field stars before using the clustering algorithm. We considered sources with a parallax cut-off of $|\varpi - \frac{1}{D}| < (3 \times \varpi_{err})$, where D is distance and ϖ_{err} is the error in parallax. This condition removes field stars in the line of sight, Vasiliev (2019). The following filtering of the data was done as below (Vasiliev 2019; Kerr *et al.* 2023):

1. AEN < 1.0,
2. RUWE < 1.2,

3. $(\mathrm{PMRA}^2 + \mathrm{PMDEC}^2) < (30.0)^2$,
4. $P_{bp\text{-}rp}(\mathrm{excess}) < 1.3 + 0.037 \times (bp\text{-}rp)^2$,
5. $\frac{\varpi}{\varpi_{err}} > 5$,

where AEN is the Astrometric Excess Noise, representing the excess noise in the sources arising from modeling errors and unresolved binaries, and RUWE is the Renormalized Unit Weight Error; a higher value of this indicates the presence of non-single stars, such as unresolved binaries and clumped-up sources. Thus, the quality filter, conditions (1) and (2), help to eliminate unreliable astrometric sources. Also, sources with very large PM are removed using the condition (3), where PMRA is the PM in the right ascension (RA) direction, and PMDEC is the PM in the declination (DEC) direction.

$P_{bp\text{-}rp}$(excess) is the photometric excess factor of a source and $bp\text{-}rp$ is the $G_{bp} - G_{rp}$ color. The $P_{bp\text{-}rp}$(excess) measures the excess flux in the integrated BP and RP integrated photometry. The condition (4) removes the faint sources that are affected by a brighter source nearby, i.e., the color of the fainter sources appears to be brighter than it actually is. An additional constraint in parallax, condition (5), is also used to remove the sources with higher errors in their parallax measurement.

2.2 *Identification of cluster members using GMM*

The crucial part of the study was to identify the cluster members. We have used the Gaussian Mixture Model (GMM) algorithm, Vasiliev (2019), for the probabilistic identification of the cluster members. The Python algorithm for GMM is available on GitHub, GaiaTools.

We used the PM information obtained from *Gaia* DR3 for the sources that pass through the filtering conditions mentioned in sub-section 2.1 to identify the cluster members using GMM. The GMM assumes several Gaussian distributions for each data group within the given data. Initial conditions, such as PM and velocity dispersion information obtained from the literature surveys, were used to initiate the algorithm to find the best-fit Gaussian parameter using the expectation-maximization algorithm. A Gaussian distribution is assumed for cluster members and field stars, and the best-fit parameters are used to find the membership probability of the individual sources.

From this analysis, we obtained revised mean values for PMRA and PMDEC, as well as their corresponding errors for a cluster. Also, the membership probability of all sources was obtained. For further analysis, we have chosen sources with a probability ≥90% as the cluster members.

Even after the probability cut off, the cluster members include fainter stars that are likely to have larger uncertainties in PM and parallax (Cantat-Gaudin *et al.* 2020). Hence, we removed the sources with their G mag ≥19. Also, an additional filtering condition is used by defining a parameter PMR_0, by which the PM of the sources varies with respect to the PM from the literature survey, Jadhav *et al.* (2021):

$$\mathrm{PMR}_0 = \sqrt{\left\{ \begin{array}{l} (\mathrm{PMRA}_s - \mathrm{PMRA}_i)^2 \\ \quad +(\mathrm{PMDEC}_s - \mathrm{PMDEC}_i)^2 \end{array} \right\}}, \tag{1}$$

where PMRA_s and PMRA_i are the PM along RA for a source and the intrinsic PMRA of the cluster, respectively. And PMDEC_s and PMDEC_i are the PM along DEC for a source and intrinsic PMDEC for the cluster, respectively. And only sources with $\mathrm{PMR}_0 < 2$ are included for further analysis.

We have also made use of the available radial velocity measurements for the cluster members from *Gaia* DR3. We used these estimations to eliminate sources having a deviation greater than 3σ from the mean radial velocity for further study.

2.3 *Isochrone fitting*

The *Gaia* color-magnitude diagram (CMD) of the clusters can be compared with isochrones to find the cluster parameters, such as age, distance, metallicity, and extinction. For that, we used the PARSEC isochrone models (Bressan *et al.* 2012; Chen *et al.* 2014, 2015). The required isochrone models were downloaded from the CMD 3.7 web interface. The ranges for $\log_{10}$(age) are set between 6.0 and 8.0 with a time step of 0.01 and metallicity ([M/H]) between −0.2 and 0.2 with a time step of 0.02. We used a combination of least-square minimization and the Markov Chain Monte Carlo (MCMC) method to fit the isochrone to the cluster CMDs, as described below.

2.3.1 Least-square minimization technique The least-square minimization was used to find the prior estimates of the parameters, such as age, distance, metallicity, and extinction, for MCMC sampling. We used the distance moduli equation to estimate the distance to the cluster and extinction in G mag:

$$M_G = m_G - \left[5 \times \log\left(\frac{D}{10}\right)\right] - A_G, \tag{2}$$

$$M(bp\text{-}rp) = (bp\text{-}rp) - 0.537 * A_G, \tag{3}$$

where M_G is the absolute G magnitude (G mag), m_G is the apparent G mag, D is the distance to the cluster, A_G is the extinction in G mag, $M(bp\text{-}rp)$ is the dereddened $bp\text{-}rp$ color, and $bp\text{-}rp$ is the color without reddening correction. The relation between reddening correction for color and extinction in G mag was obtained from the CMD 3.7 website, Cardelli *et al.* (1989) and O'Donnell (1994).

The least-square minimization algorithm finds the theoretical model that shows a close match with cluster members in their CMD. The $\log_{10}$(age) was varied by ± 0.5 with a step size of 0.05 and distance by ± 10 pc with a step size of 1 pc from the $\log_{10}$(age) and distance obtained from the literature survey, respectively. Metallicity ([M/H]) was varied between -0.2 and 0.2 dex with a step size of 0.1 dex, and A_G was varied between 0 and 0.832 with a step size of 0.1:

$$S = S_{\text{mag}} + S_{\text{color}}, \tag{4}$$

where

$$S_{\text{mag}} = (M_{G,i} - M_{G,j})^2, \tag{5}$$

$$S_{\text{color}} = [M(bp\text{-}rp)_i - M(bp\text{-}rp)_j]^2, \tag{6}$$

where $M_{G,i}$ and $M_{G,j}$ represent the absolute G mag of cluster members and the isochrone model, respectively, and $M(bp\text{-}rp)_i$ and $M(bp\text{-}rp)_j$ represent the reddening corrected $bp\text{-}rp$ color of cluster members and the isochrone model, respectively. By varying parameters as mentioned above, we found the deviation (S) of each model from our cluster members using the above equation. Then, we also removed the data points having a higher deviation from the CMD by using 1σ clipping and chose only those points that passed the sigma clipping for fitting. Next, we found the mean deviation of these chosen points. The prior estimates were found by finding the model with the least mean deviation. These estimated parameters will provide us with the prior estimates for age, metallicity, distance, and extinction in the G mag of the desired cluster.

2.3.2 MCMC technique The prior estimates obtained from the previous step are then used as the initial guesses for each cluster to run the MCMC, Hogg & Foreman-Mackey (2018). We have used the emcee Python library, Foreman-Mackey *et al.* (2013), for this purpose. For a better MCMC performance, we required isochrone models with better resolution. Since the step size of the models generated from PARSEC is smaller, we defined a function that could generate isochrones for any given random values of $\log_{10}$(age), [M/H], distance, and extinction. This synthetic generation of isochrones was achieved by a series of linear interpolations of the downloaded theoretical isochrones from PARSEC. Firstly, the interpolation was done with respect to their age and then with respect to their metallicity to obtain the desired isochrone. Also, the time step mentioned in sub-section 2.3.1 for $\log_{10}$(age) is increased from 0.05 to 0.01 dex, and that of [M/H] from 0.1 to 0.02. This ensures that the generated synthetic isochrones are more precise.

We defined the likelihood function as,

$$\ln L = -\frac{1}{2}\sum \Big\{ \chi^2_{\text{mag}} + \chi^2_{\text{color}} + \log(m_{Gerr,i}) + \log[(bp\text{-}rp)_{err,i}] \Big\}, \tag{7}$$

where

$$\chi^2_{\text{mag}} = \frac{(m_{G,i} - m_{G,j})^2}{m_{Gerr,i}}, \tag{8}$$

$$\chi^2_{\text{color}} = \frac{[(bp\text{-}rp)_i - (bp\text{-}rp)_j]^2}{(bp\text{-}rp)_{err,i}}, \tag{9}$$

where $m_{G,i}$ and $m_{G,j}$ represent the apparent G mag of cluster members and the isochrone model, respectively, and $(bp\text{-}rp)_i$ and $(bp\text{-}rp)_j$ represent the apparent $(bp\text{-}rp)$ color of cluster members and isochrone model, respectively. While $m_{Gerr,i}$ and $(bp\text{-}rp)_{err,i}$ are the errors in the G mag and $(bp\text{-}rp)$ color of the cluster members, respectively.

Since there is a spread of cluster members in the CMD, it is challenging to implement MCMC. Hence, we used fiducial points instead of the full CMD in the cluster sequence. This fiducial point is obtained by binning the cluster members with respect to G mag with a bin size of 0.1 mag. Then, we removed the highly deviated data points in each bin by giving a sigma clipping of 3σ in the $(bp\text{-}rp)$ color. Next, we found the mean G mag and $(bp\text{-}rp)$ color and their corresponding error using the clipped data points. The CMD obtained by plotting the mean G mag and $(bp\text{-}rp)$ is the fiducial sequence for our cluster members. This is then used to fit the theoretical isochrones. Uniform priors were chosen such that they centered around the parameter values obtained from sub-section 2.3.1.

Then, by giving initial guesses as prior estimates from sub-section 2.3.1, we ran MCMC with 72 walkers and a step size of 500 steps. We set the initial 250 steps as the burn-in phase and found all clusters to have converging parameters afterward, and then found the 16th, 50th, and 84th percentiles. We took the 50th percentile as the best-fit parameter for each parameter space. The difference between the 16–50th and the 50–84th percentiles are taken as the errors for these best-fit parameters.

2.4 *Velocity estimation*

The transverse velocity, which is the velocity along the perpendicular component to our line of sight of a star, can be determined from the PM of a star:

$$V_T = 4.74\ (\mu D), \tag{10}$$

where V_T is the transverse velocity in km s^{-1}, μ is the PM in milliarcseconds per year (mas yr^{-1}), and D is the distance from the sun in kiloparsec (kpc) of a star. By substituting for the distance obtained from the MCMC method, we found the mean transverse velocity for each cluster. Its dispersion was then found by taking its standard deviation.

We found the mean radial velocity of clusters using the radial velocity measurements of the members from *Gaia* DR3 data.

Space velocity is the total velocity experienced by a cluster in 3D space. It is obtained by considering the mean radial velocity and the mean transverse velocity.

$$V = \sqrt{V_T^2 + V_R^2}, \tag{11}$$

where V is the space velocity, V_T is the transverse velocity, and V_R is the radial velocity.

2.5 *Mass estimation*

Photometric masses for the stars were available in the PARSEC isochrone data (Bressan *et al.* 2012; Chen *et al.* 2014, 2015). We used a similar interpolation method mentioned in sub-section 2.3.2 to obtain the mass sequence for the best-fit isochrone. Which was then further interpolated with respect to the G mag of the cluster members to obtain the mass of individual stars within the cluster.

3. Results and discussion

3.1 *Membership information*

We have determined members of stars belonging to the 14 clusters using GMM as mentioned in the sub-section 2.2. The number of stars belonging to each cluster is mentioned in Table 1 and the cluster parameters obtained for each cluster using GMM are shown in Table 1.

Spatial plots were plotted to study the spatial distribution of each cluster, which is shown in Figure 1. We note that the clusters are located in regions with a wide range of field contamination. Vector Point Diagrams (VPDs) show the PM distribution of cluster members along with the field stars (Figure 2). From the VPDs, we can see that all the cluster members are identified as a compact group with cluster members having similar PMs. The PM of the field stars shows a range. It is interesting to note the paucity of field stars near the cluster NGC 1980. On the other hand, we note a large population of field stars in the field of Collinder 132 and UBC 26.

Table 1. Cluster parameters obtained for each cluster using GMM. Columns 2 and 3 are the two components of PM along with their errors. N_{star} represents the number of sources with probability ≥90%.

Cluster name	pmra (mas yr^{-1})	pmdec (mas yr^{-1})	N_{star}
Alessi 24	-0.441 ± 0.012	-8.95 ± 0.013	135
Alessi Teutsch 12	-2.324 ± 0.046	-8.907 ± 0.045	22
ASCC 58	-13.262 ± 0.02	2.793 ± 0.02	123
Alessi Teutsch 5	-1.868 ± 0.031	-3.317 ± 0.027	118
ASCC 16	1.348 ± 0.017	-0.097 ± 0.017	280
ASCC 21	1.458 ± 0.018	-0.491 ± 0.018	223
Collinder 69	1.216 ± 0.018	-2.134 ± 0.017	517
Collinder 132	-4.006 ± 0.033	3.698 ± 0.029	186
IC 2395	-4.426 ± 0.011	3.307 ± 0.011	329
ASCC 127	7.471 ± 0.02	-1.813 ± 0.021	113
NGC 1980	1.173 ± 0.031	0.374 ± 0.031	249
Roslund 5	2.056 ± 0.013	-1.212 ± 0.013	151
UBC 26	2.09 ± 0.018	-5.272 ± 0.018	140
NGC 6405	-1.389 ± 0.013	-5.874 ± 0.011	641

The number of cluster members estimated from our study is lower than that estimated by Cantat-Gaudin *et al.* (2020) except for 7 OCs (ASCC 16, ASCC 21, Collinder 132, IC 2395, NGC 1980, UBC 26, NGC 6405), Table A2. This difference in numbers can be due to the inclusion of fainter sources between G mag = 18 and 19 in our study, while Cantat-Gaudin *et al.* (2020) has only considered stars brighter than G mag = 18. A comparison of the number of stars brighter than G mag = 18 with the literature study is shown in Figure A1. NGC 6405 was studied by Gao (2018) using a combined method of GMM and random forest to compute membership probabilities using *Gaia* GR2, and identified 581 members. In this study, 641 members were identified using *Gaia* DR3 data.

3.2 *Cluster parameters*

CMDs are used to estimate the cluster parameters, such as age, distance, metallicity, and extinction. PARSEC isochrones were fitted against the CMD for each cluster for this estimation, sub-section 2.3. The parameters

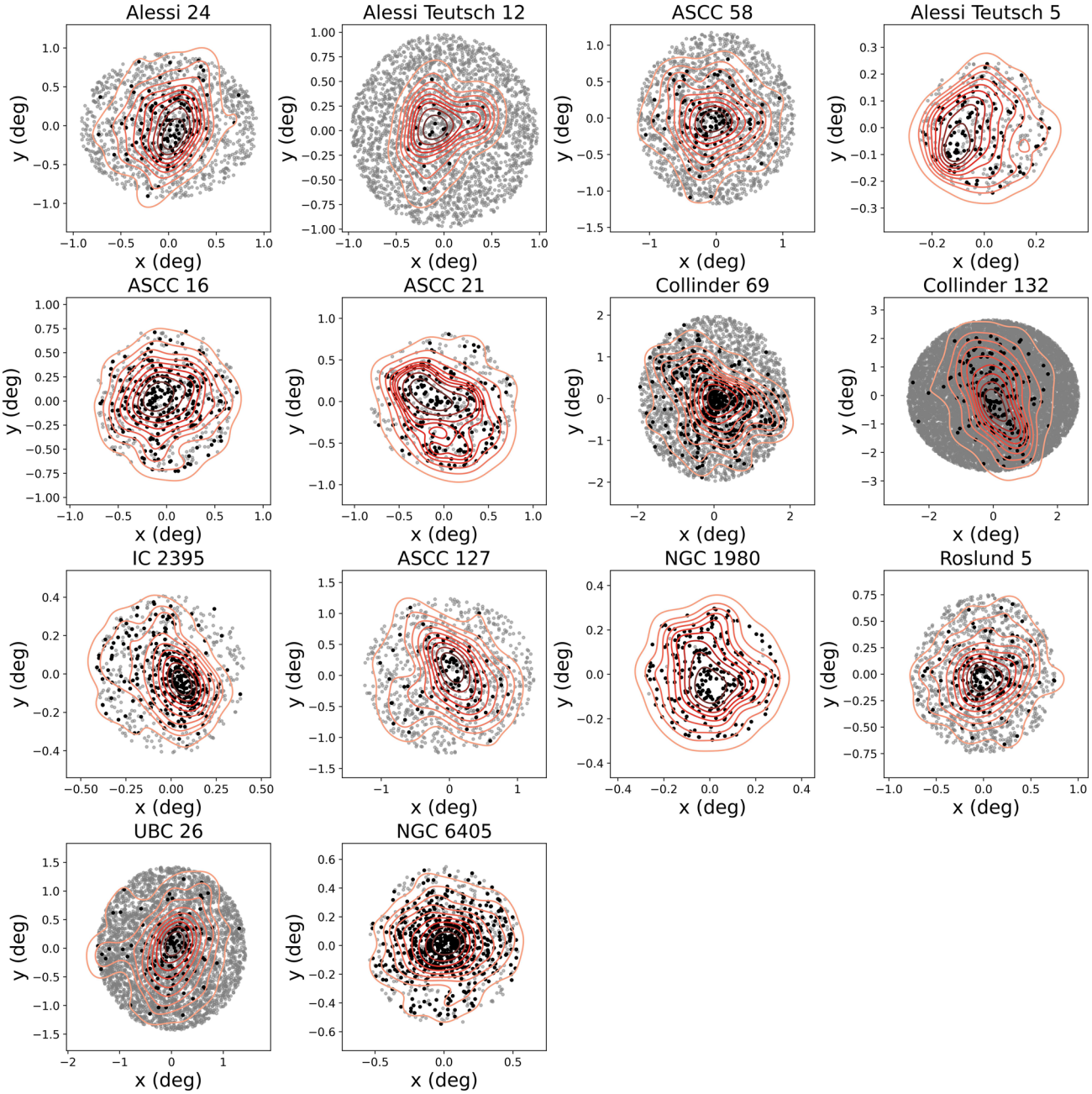

Figure 1. Spatial plot for all the OCs. Black and gray dots represent the cluster members and field stars, respectively. The red line represents the isodensity contours.

estimated by least-square minimization and MCMC are tabulated in Table 2. The estimated parameters are closer to the values estimated by Cantat-Gaudin *et al.* (2020). We have also overplotted the CMD and best-fit isochrone to visualize the credibility of the isochrone-fitting method we used. And the isochrone fitted images for least-square minimization and the MCMC methods are shown in Figures 3 and 4, respectively.

We used the evolutionary information available in the isochrone data to classify the cluster members into pre-main-sequence (PMS) and main-sequence (MS) stars. We could see that the majority of stars within each cluster are PMS stars, and very few members are in the MS phase, Figure 3, confirming these are all young clusters. The age of the clusters ranges from 7 Myr (Alessi Teutsch 5) to 89 Myr (Roslund 5). Out of the 14 OCs studied, Alessi Teutsch 5 ($910.018^{+0.039}_{-0.024}$ pc) is the farthest, while ASCC 16 ($334.002^{+0.010}_{-0.009}$ pc) is the closest one (see Table 2). The estimated error of the parameters is lower as we used fiducial points to fit MCMC, assuming that there is no spread in the data set.

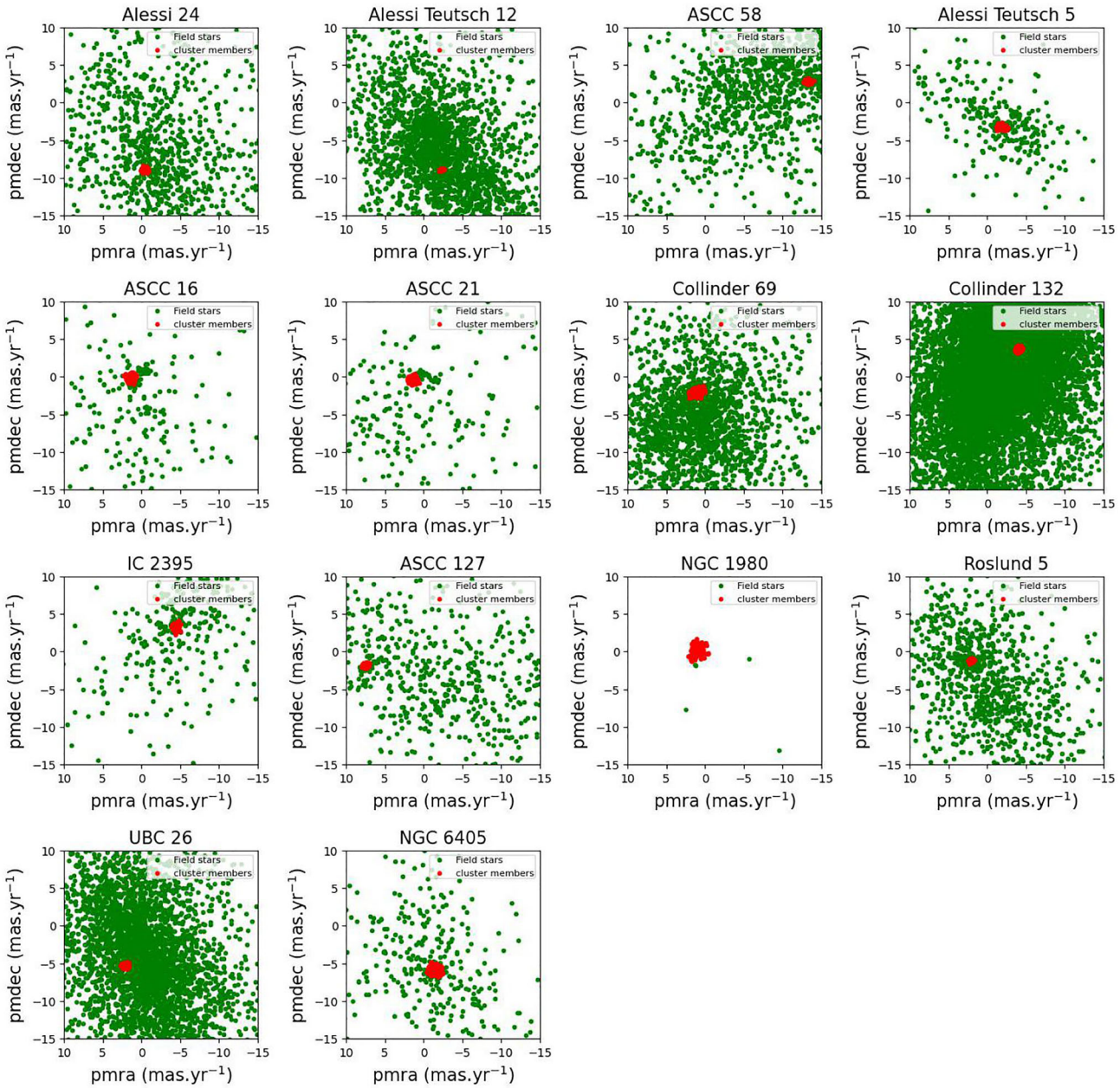

Figure 2. Vector point diagram (VPD) for all the OCs. Red and green dots represent the cluster members and field stars, respectively.

The cluster parameters estimated for the OCs, as shown in Table A2, are compared to previous studies, Figure A1. The distance and age estimates are comparable to the values of Cantat-Gaudin *et al.* (2020) and Dias *et al.* (2021). A higher difference in the parameters estimated compared to Kharchenko *et al.* (2016) can be due to the difference in the data set used and probable contamination from field stars. With the increased precision of *Gaia* DR3 data, the parameters derived in this study can be considered as better estimates for these clusters.

3.3 *Velocity*

Transverse velocity and its dispersion were then determined using the best-fit parameter obtained for distance from isochrone fitting by using the equation mentioned in sub-section 2.4. The result for this is tabulated in Table 3. From the analysis, we found that the dispersion in transverse velocity for the Alessi Teutsch 5 cluster is >1 km s^{-1}. All the other clusters have transverse velocity dispersion in the range of 0.28–0.70 km s^{-1}. Literature estimations of transverse velocity dispersion

Table 2. Isochrone fitting results from least-square minimization and MCMC. D, $\log_{10}$(age), [M/H], and A_G are the distance, $\log_{10}$(age), metallicity, and extinction in G mag, respectively, for least-square minimization and MCMC.

	Least-square minimization				MCMC			
Cluster name	D (pc)	$\log_{10}$(age) (dex)	[M/H] (dex)	A_G (mag)	D (pc)	$\log_{10}$(age) (dex)	[M/H] (dex)	A_G (mag)
Alessi 24	507	7.8	0.2	0.2	$500.160^{+0.970}_{-0.811}$	$7.795^{+0.001}_{-0.002}$	$0.211^{+0.002}_{-0.001}$	$0.135^{+0.005}_{-0.005}$
Alessi Teutsch 12	649	7.8	0.1	0.3	$646.998^{+0.015}_{-0.020}$	$7.788^{+0.004}_{-0.007}$	$0.092^{+0.013}_{-0.013}$	$0.201^{+0.022}_{-0.009}$
ASCC 58	491	7.6	0	0.3	$490.998^{+0.100}_{-0.185}$	$7.601^{+0.005}_{-0.006}$	$-0.003^{+0.008}_{-0.003}$	$0.285^{+0.017}_{-0.013}$
Alessi Teutsch 5	910	6.9	0	0.8	$910.018^{+0.039}_{-0.024}$	$6.886^{+0.001}_{-0.016}$	$0.059^{+0.001}_{-0.036}$	$0.725^{+0.017}_{-0.011}$
ASCC 16	334	7.15	−0.1	0.4	$334.002^{+0.010}_{-0.009}$	$7.157^{+0.005}_{-0.020}$	$-0.104^{+0.010}_{-0.007}$	$0.403^{+0.019}_{-0.011}$
ASCC 21	349	6.95	−0.1	0.2	$350.006^{+0.010}_{-0.013}$	$7.021^{+0.011}_{-0.001}$	$-0.107^{+0.016}_{-0.001}$	$0.193^{+0.006}_{-0.018}$
Collinder 69	425	6.6	−0.2	0.3	$418.243^{+0.047}_{-0.069}$	$7.011^{+0.016}_{-0.057}$	$0.172^{+0.062}_{-0.071}$	$0.335^{+0.014}_{-0.009}$
Collinder 132	628	7.45	0.1	0.2	$628.000^{+0.031}_{-0.040}$	$7.445^{+0.031}_{-0.013}$	$0.092^{+0.032}_{-0.004}$	$0.204^{+0.008}_{-0.023}$
IC 2395	704	6.9	−0.2	0.5	$704.001^{+0.006}_{-0.008}$	$6.897^{+0.005}_{-0.001}$	$-0.204^{+0.009}_{-0.000}$	$0.504^{+0.002}_{-0.002}$
ASCC 127	383	7	−0.2	0.6	$350.944^{+13.498}_{-3.142}$	$7.147^{+0.001}_{-0.001}$	$-0.254^{+0.004}_{-0.001}$	$0.724^{+0.019}_{-0.053}$
NGC 1980	369	6.95	−0.1	0.3	$351.984^{+6.310}_{-4.238}$	$6.940^{+0.008}_{-0.008}$	$-0.159^{+0.009}_{-0.005}$	$0.382^{+0.076}_{-0.078}$
Roslund 5	555	7.9	0.2	0.3	$555.011^{+0.009}_{-0.017}$	$7.946^{+0.008}_{-0.003}$	$0.194^{+0.016}_{-0.022}$	$0.309^{+0.010}_{-0.018}$
UBC 26	573	7.5	0.2	0.8	$578.684^{+0.020}_{-0.012}$	$7.482^{+0.023}_{-0.028}$	$0.211^{+0.034}_{-0.028}$	$0.771^{+0.025}_{-0.016}$
NGC 6405	468	7.7	0.2	0.5	$468.003^{+0.020}_{-0.022}$	$7.697^{+0.009}_{-0.002}$	$0.193^{+0.018}_{-0.005}$	$0.469^{+0.004}_{-0.005}$

of OCs suggest that they are generally $\leq$2 km s^{-1} (McNamara & Sekiguchi 1986; Sagar & Bhatt 1989). Recently, Kulesh *et al.* (2024) estimated the velocity dispersion along the Right Ascension and Declination for NGC 2571 to be ∼0.55 km s^{-1}. We note that the transverse velocity dispersion for most of the clusters is in this range.

We also estimated the space velocity of each cluster by using the radial velocity information available in *Gaia* DR3 as mentioned in sub-section 2.4, Table 3. Since measurement error overpowers the standard error of radial velocity, we have used measurement error for the error determination of space velocity. Also, due to the limited amount of information on radial velocity available, the calculated space velocity can have a higher error than the calculated one. From the analysis, ASCC 16 has the lowest space velocity of 12.96 ± 0.04 km s^{-1}, and ASCC 58 has the highest space velocity of 34.59 ± 0.01 km s^{-1}.

3.4 *Mass dependency of velocity dispersion*

We classified cluster members based on their spectral type (O, B, A, F, G, K, and M) by using the updated version of Erik Mamajek's table, Pecaut & Mamajek (2013). This is achieved by comparing the G mag range for each spectral type in the table to the G mag values of our cluster members. They are grouped into BA, FG, K, and M-type stars since the number of stars in the high-massive stars (B, A, F, G) is much lower compared to low-massive stars (K and M). The mass of the group is obtained by taking the mean mass of stars within a group, and the obtained results are tabulated in Table 4. The transverse velocity dispersion of each group is determined by taking the standard deviation of transverse velocity within each group and its error as standard error, Table 4.

Within the mass range of 1.0–0.5 $M_\odot$, 5 clusters show a statistically significant increase in the transverse velocity dispersion, Figure 5. We consider these as statistically significant increases as their error range does not overlap with the mean value of other groups within 2 sigma. These are Collinder 132, NGC 1980, IC 2395, ASCC 58, and Alessi 24. The other clusters either show no trend or the increase is not statistically significant. The increasing velocity dispersion is indicative of kinematic relaxation with the presence of equipartition activity in the cluster. The clusters have a large range in age (8–63 Myr) and have a range in the number of member stars (123–329 members). The evidence

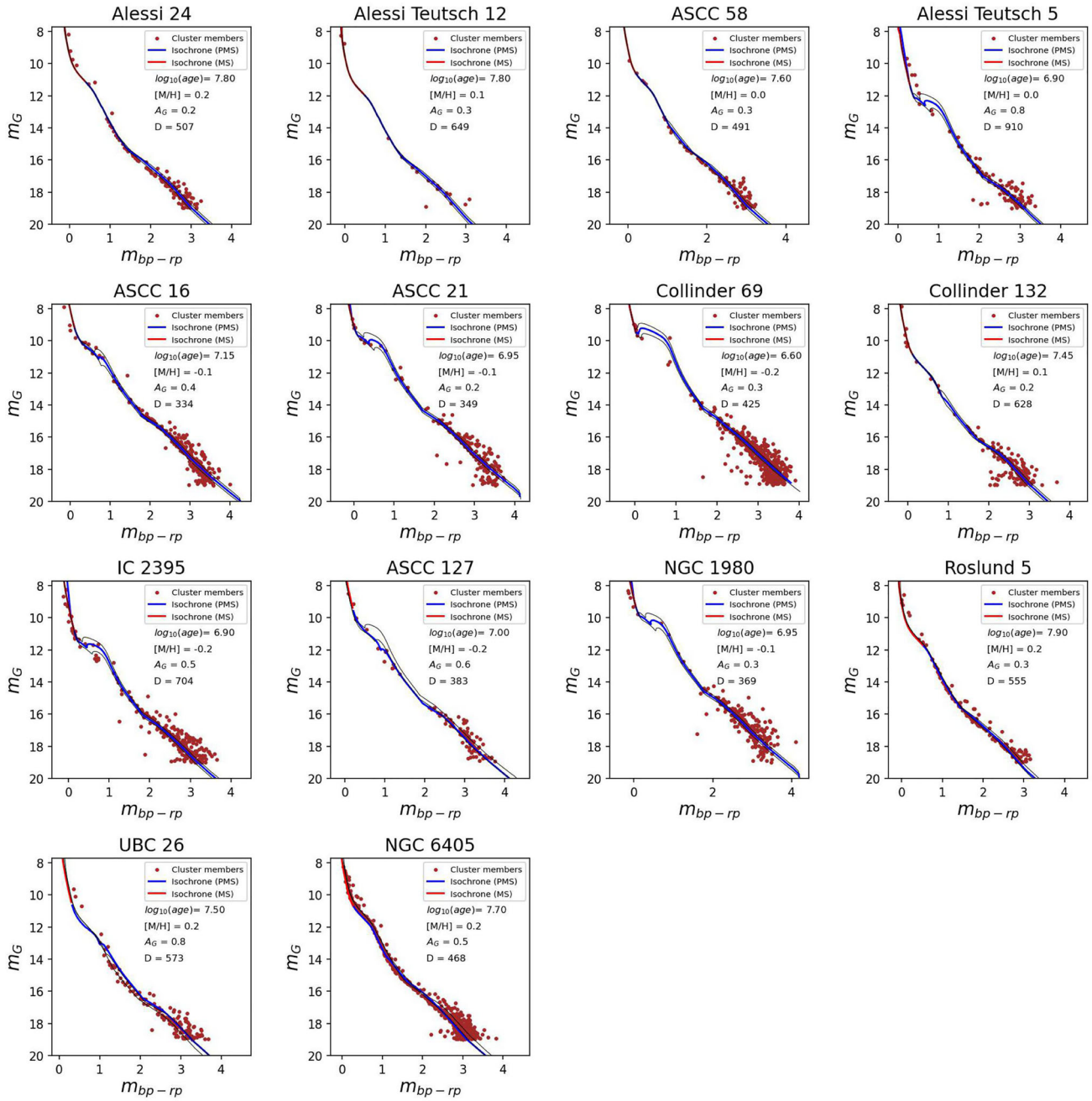

Figure 3. Isochrone-fitting using least-square minimization for all the OCs. Here, brown dots represent the cluster members; the blue line represents the isochrone for pre-main-sequence (PMS) stars, and the red line represents the isochrone for main-sequence (MS) stars. Also, $\log_{10}$(age), metallicity (M/H), distance (D) in PC, and extinction in G mag (A_G) estimated from isochrone fitting are mentioned in the plots. The black lines represent isochrone with $\log_{10}$(age) $\pm$ 0.1.

of relaxation for low-mass stars in young clusters, such as IC 2395 (8 Myr) and NGC 1980 (9 Myr) are interesting. A similar work was carried out by Sagar & Bhatt (1989) and McNamara & Sekiguchi (1986) to study the internal kinematics of the OCs. A statistically significant increase in transverse velocity dispersion as mass decreases also points to the mass segregation within OCs. The Alessi 24 OC was studied by Bhattacharya *et al.* (2022), where they indicated the possibility of slight mass segregation, which agrees with our findings based on velocity dispersion.

3.5 *High PM massive stars*

In general, low-mass stars show relatively higher velocity dispersion than high-mass stars. Apart from this, in

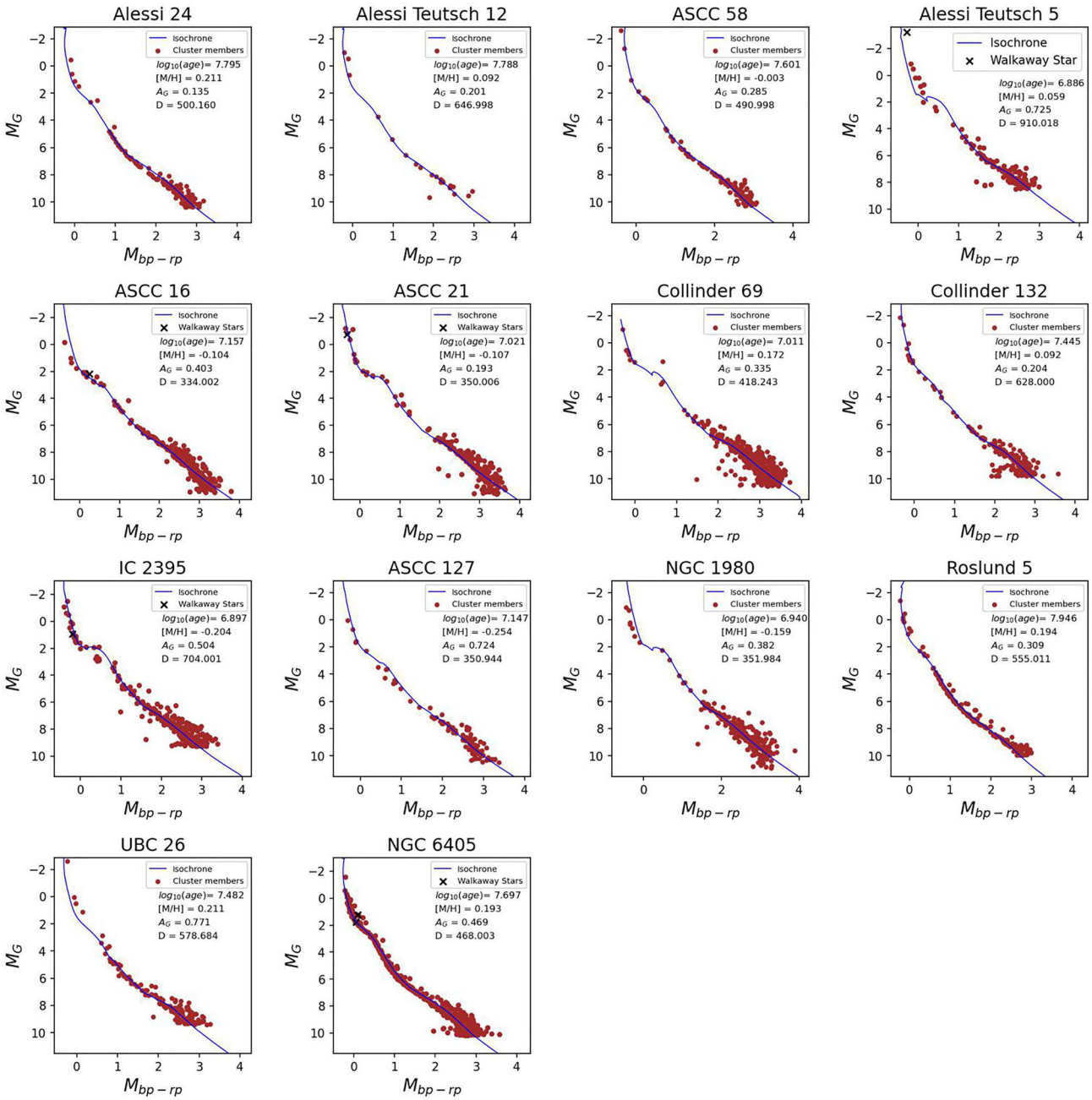

Figure 4. Isochrone-fitting using MCMC for all the OCs. Here, brown dots represent the cluster members; the blue line represents the isochrone, and the black cross represents the possible walkaway stars.

some clusters, even the high-mass stars appear to show relatively large velocity dispersion. This deviation in high-mass stars not following the velocity-mass relation is in agreement with Sagar & Bhatt (1989) and McNamara & Sekiguchi (1986).

Some clusters are found to have BA-type stars with relatively large PM, as shown in Figure 6. These are the ones having a transverse velocity greater than 2σ from the mean transverse velocity of the OCs. These are found in 5 clusters (Alessi Teutsch 5, ASCC 16, ASCC 21, IC 2395, and NGC 6405), and all these clusters are in the age range of 8–15 Myr, except NGC 6405. NGC 6405 (49–50 Myr) is an older cluster, and it has two such stars. The relative velocity of these stars ranges from 0.86 to 3.3 km s^{-1}. Also, the mass of these stars ranges between 1.7 and 13.7 $M_{\odot}$. The star with the highest relative transverse velocity is seen in Alessi Teutsch 5 (3.3 km s^{-1}), which has a mass of 13 $M_{\odot}$ (B-type star). The locations of these stars are shown in the Figure 7. Many are found in the central regions of these young

Table 3. Radial velocity and space velocity estimation for the clusters. N_{RV} represents the number of stars in a cluster with radial velocity information available in the *Gaia* DR3. Columns 3–6 represent the radial velocity mean and its dispersion, standard error, and measurement error, respectively. N_{star} is the number of cluster members. Columns 8–10 are the transverse velocity mean, its dispersion, and standard error, respectively. Columns 11 and 12 represent the space velocity and its error.

Cluster name	N_{RV}	RV_mean (km s^{-1})	RV_disp (km s^{-1})	RV_std_er (km s^{-1})	RV_er (km s^{-1})	N_{star}	Tvel_mean (km s^{-1})	Tvel_disp (km s^{-1})	Tvel_std_er (km s^{-1})	Space_V (km s^{-1})	Space_V_er (km s^{-1})
Alessi 24	17	10.20	4.89	1.19	4.12	135	21.25	0.43	0.04	23.57	0.02
Alessi Teutsch 12	3	−3.95	3.33	1.92	4.86	22	28.26	0.28	0.06	28.54	0.04
ASCC 58	14	14.15	11.34	3.03	4.74	123	31.57	0.47	0.04	34.59	0.01
Alessi Teutsch 5	6	0.27	28.41	11.60	11.45	118	16.68	1.22	0.11	16.68	2.53
ASCC 16	55	12.77	16.26	2.19	5.93	280	2.20	0.43	0.03	12.96	0.04
ASCC 21	37	13.74	25.49	4.19	6.01	223	2.59	0.38	0.03	13.98	0.03
Collinder 69	37	17.85	22.59	3.71	6.85	517	4.88	0.67	0.03	18.51	0.02
Collinder 132	17	21.75	5.40	1.31	5.00	186	16.50	0.65	0.05	27.30	0.01
IC 2395	35	24.34	17.76	3.00	8.06	329	18.39	0.70	0.04	30.50	0.01
ASCC 127	16	−13.86	16.93	4.23	4.40	113	12.81	0.33	0.03	18.87	0.02
NGC 1980	36	22.30	24.54	4.09	6.21	249	2.28	0.56	0.04	22.42	0.01
Roslund 5	38	−17.53	5.51	0.89	4.05	151	6.32	0.41	0.03	18.63	0.01
UBC 26	14	−15.12	13.34	3.56	4.68	140	15.65	0.57	0.05	21.76	0.01
NGC 6405	164	−11.06	8.81	0.69	4.60	641	13.43	0.69	0.03	17.40	0.02

Table 4. Transverse velocity and its dispersion for each spectral type. Columns 2–5 represent the mean mass of each spectral type, and columns 6–9 represent the dispersion in transverse velocity along with their errors for the mentioned group of spectral types.

Cluster name	Mass_BA ($M_\odot$)	Mass_FG ($M_\odot$)	Mass_K ($M_\odot$)	Mass_M ($M_\odot$)	BA_Tvel_disp (km s^{-1})	FG_Tvel_disp (km s^{-1})	K_Tvel_disp (km s^{-1})	M_Tvel_disp (km s^{-1})
Alessi 24	3.6	1.21	0.74	0.47	0.21 ± 0.09	0.21 ± 0.08	0.29 ± 0.06	0.47 ± 0.05
Alessi Teutsch 12	4.55	1.11	0.68	0.53	0.19 ± 0.09	0.29 ± 0.2	0.19 ± 0.09	0.31 ± 0.09
ASCC 58	3.45	1.11	0.72	0.43	0.38 ± 0.15	0.18 ± 0.08	0.31 ± 0.07	0.5 ± 0.05
Alessi Teutsch 5	4.24	1.26	0.65	0.45	1.44 ± 0.46	1.06 ± 0.3	1.03 ± 0.12	1.67 ± 0.36
ASCC 16	3.04	1.29	0.68	0.31	0.4 ± 0.12	0.29 ± 0.08	0.34 ± 0.04	0.46 ± 0.03
ASCC 21	3.99	1.23	0.64	0.29	0.35 ± 0.09	0.28 ± 0.1	0.32 ± 0.05	0.4 ± 0.03
Collinder 69	3.11	1.31	0.7	0.34	0.44 ± 0.15	0.49 ± 0.22	0.6 ± 0.05	0.69 ± 0.04
Collinder 132	3.32	1.27	0.73	0.47	0.26 ± 0.08	0.27 ± 0.09	0.56 ± 0.09	0.69 ± 0.06
IC 2395	3.17	1.26	0.58	0.32	0.78 ± 0.17	0.47 ± 0.09	0.61 ± 0.05	0.79 ± 0.06
ASCC 127	2.59	1.11	0.62	0.29	0.14 ± 0.06	0.26 ± 0.09	0.31 ± 0.06	0.35 ± 0.04
NGC 1980	4.62	1.21	0.6	0.28	0.54 ± 0.18	0.27 ± 0.11	0.52 ± 0.05	0.59 ± 0.05
Roslund 5	3.08	1.17	0.74	0.49	0.31 ± 0.1	0.35 ± 0.07	0.35 ± 0.05	0.49 ± 0.06
UBC 26	4.25	1.13	0.76	0.53	0.49 ± 0.25	0.56 ± 0.15	0.46 ± 0.07	0.6 ± 0.07
NGC 6405	2.63	1.23	0.76	0.47	0.67 ± 0.09	0.62 ± 0.07	0.61 ± 0.06	0.72 ± 0.04

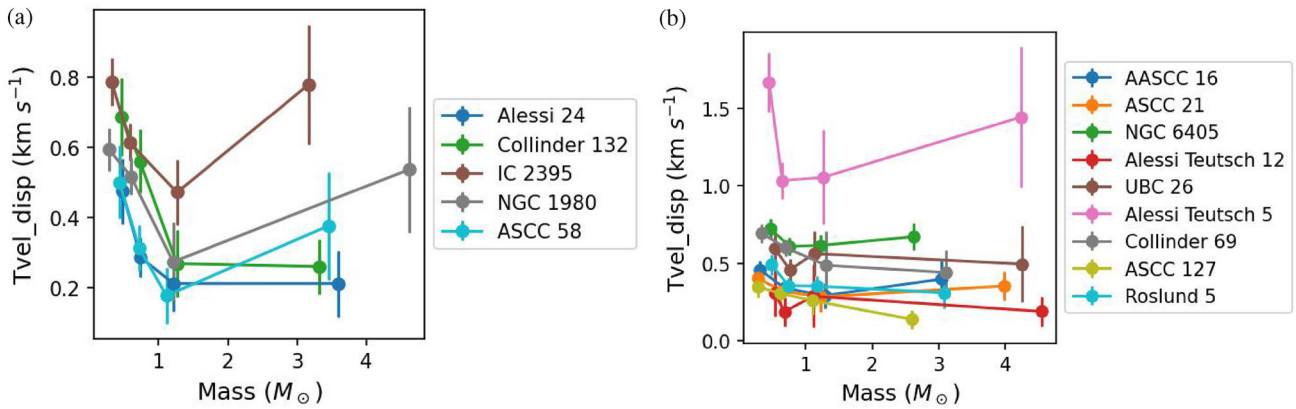

Figure 5. Mass vs. transverse velocity dispersion. (a) Statistically significant ones and (b) may have statistical insignificance.

clusters. These are potential candidates to escape the cluster potential. Fujii & Portegies Zwart (2011) suggested that the dynamically ejected runaway stars are generally produced in the dense regions of clusters. It is possible that dynamic effects are at work in these 5 clusters and are responsible for the creation of these large PM massive stars. It is also possible that some high-velocity stars have left the cluster already. We suggest that these stars can be possible walkaway stars, which might move out of the cluster in the future.

3.6 *Fraction of M- to K-type stars*

Though we have the membership and mass range of stars, due to incompleteness and poor statistics, it may not be appropriate to estimate the Initial Mass Function (IMF) of these clusters. There are many studies that are dedicated to studying the IMF in young clusters, such as Damian *et al.* (2021), Luhman *et al.* (2016), and Suárez *et al.* (2019). On the other hand, we do have a good number of stars in the K and M spectral types, which could be used to check the fraction of stars expected, particularly, near the transition mass of ∼0.4–0.5 $M_\odot$. This can throw light on possible reasons for the variation in the number of stars in the K and M spectral types as seen in the Table 5. We estimated the present-day M/K ratio for all clusters and compared the value with that expected from: (1) Salpeter slope for initial mass function (−2.35 for both M and K type stars, Salpeter, 1955) and (2) Kroupa slope for the initial mass function (−1.3 for $M_\odot < 0.5$ and −2.3 for $M_\odot > 0.5$, Kroupa, 2001). The observed M/K values can be the lower bound values

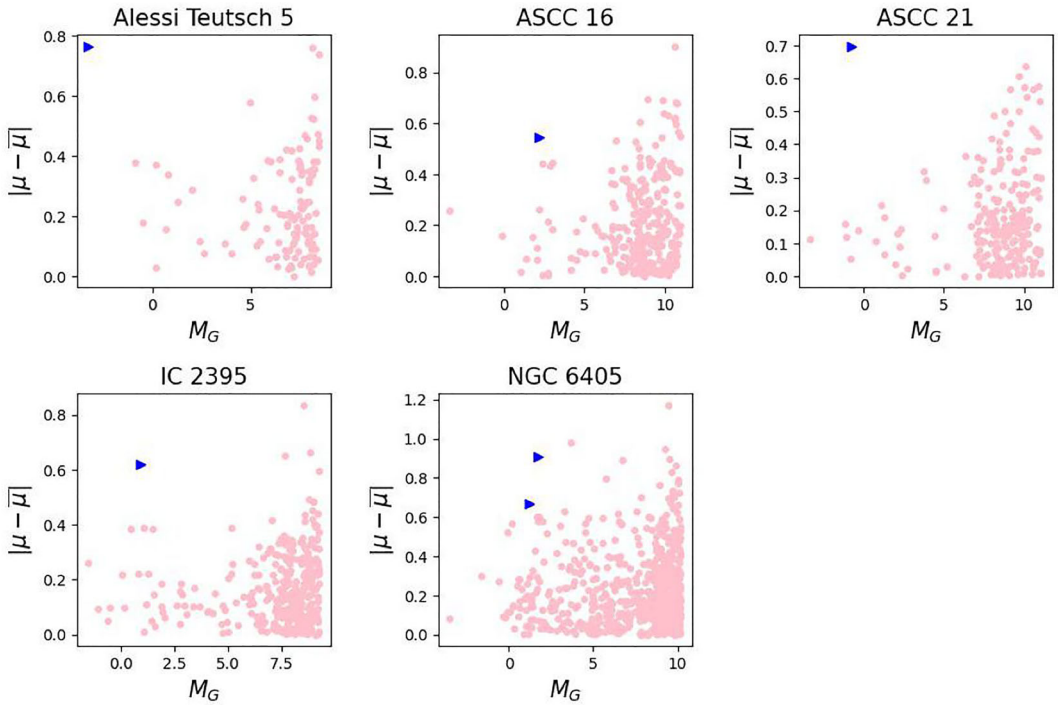

Figure 6. Clusters with higher massive stars having relatively large variations in their PM. Blue triangle representing the star with higher variation in the PM.

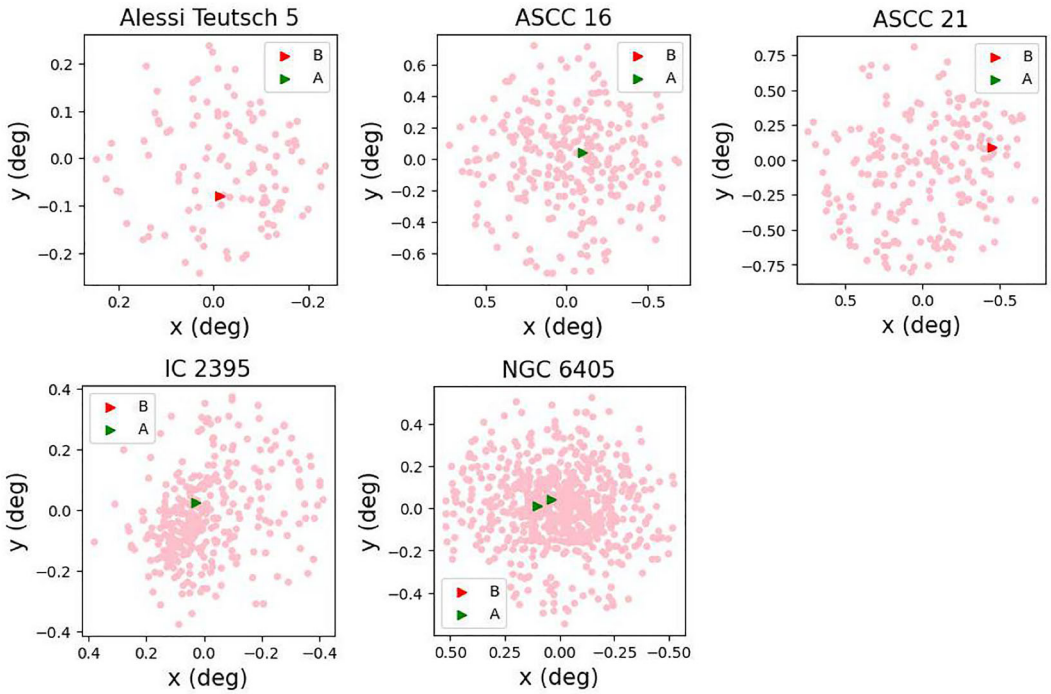

Figure 7. Spatial plot of clusters with possible walkaway stars detected. The triangle represents the position of stars with higher variation in PM. The red and green triangles represent the B- and A-type stars, respectively

due to the, incompleteness of the data set. By definition, the expected ratio for Salpeter IMF is higher than that for Kroupa IMF (Figure 8).

Alessi Teutsch 5 has a ratio <1, probably, because of missing low mass stars due to its large distance. Furthermore, due to the presence of another cluster

Table 5. Spectral type classification of cluster members. Columns 2–7 represent the number of sources belonging to each spectral type for the corresponding clusters mentioned in column 1. Columns 8 and 9 represent the mass range of the cluster, with Mass_min representing the minimum mass and Mass_max representing the maximum mass in solar mass ($M_\odot$). Column 10 represents the observed ratio of M-type stars to the K-type stars in the corresponding clusters, which are the lower bound values. Columns 11 and 12 represent expected M/K ratios from Salpeter (Salpeter 1955) and Kroupa (Kroupa 2001), respectively.

Cluster name	B	A	F	G	K	M	Mass_min ($M_\odot$)	Mass_max ($M_\odot$)	M/K	M/K Salpeter	M/K Kroupa
Alessi 24	3	2	2	5	26	97	0.33	6.23	≥3.73	2.84	1.32
Alessi Teutsch 12	4	0	1	1	4	12	0.43	6.28	≥3.00	1.77	1.75
ASCC 58	2	4	1	4	23	89	0.28	7.19	≥3.87	3.41	1.42
Alessi Teutsch 5	7	3	3	9	75	21	0.41	13.01	≥0.28	2.37	1.05
ASCC 16	2	9	8	5	63	193	0.15	11.71	≥3.06	6.28	1.89
ASCC 21	7	8	3	5	47	153	0.13	12.89	≥3.26	6.62	1.81
Collinder 69	5	4	2	3	127	376	0.20	5.70	≥2.96	5.31	1.75
Collinder 132	4	7	6	2	38	129	0.33	6.87	≥3.39	2.87	1.31
IC 2395	8	13	12	14	135	147	0.25	7.41	≥1.09	4.06	1.27
ASCC 127	2	3	3	5	24	76	0.16	3.93	≥3.17	6.01	1.67
NGC 1980	6	3	2	4	97	137	0.13	13.77	≥1.41	5.73	1.57
Roslund 5	7	3	10	17	51	63	0.41	4.77	≥1.24	2.63	1.27
UBC 26	3	1	5	10	41	80	0.42	7.70	≥1.95	2.33	2.29
NGC 6405	19	43	42	43	119	375	0.34	7.12	≥3.15	3.04	1.41

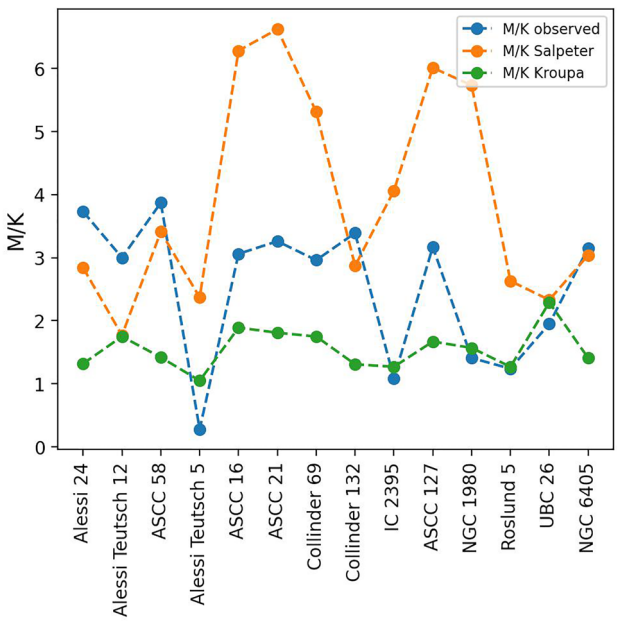

Figure 8. Comparison of M/K ratio to the ratios of Salpeter and Kroupa.

(BDSB 30), (Cantat-Gaudin *et al.* 2020), closer to Alessi Teutsch 5, we restricted our study to a lower radius, which might also contribute to this lower ratio.

UBC 26 is a nearby young cluster, and the observed and expected ratios are similar. IC 2395, NGC 1980, and Roslund 5 have their ratio similar to the Kroupa ratio (Figure 8). The M/K ratio estimated for ASCC 16, ASCC 21, ASCC 127, and Collinder 69 appears to be between that expected from Salpeter and Kroupa IMFs. We expect these ratios might actually be higher than the ones we found, as the M/K ratio we found represents the lower bound. The ratios estimated for Alessi 24, ASCC 58, and Collinder 132 appear to be higher than those expected from even Salpeter IMF, Figure 8. These clusters are older, with ages in the range of 28–62 Myr. NGC 6405 is an older cluster with a ratio similar to that expected from the Salpeter IMF. A detailed study needs to be performed to validate this, and we plan to carry this out in the future.

3.7 *Structural study of clusters*

An elongated structure is seen for Alessi 24, Collinder 132, ASCC 127, and UBC 26, Figure 9, with an age range of 14–62 Myr. These clusters are comparatively older (28–62 Myr) except ASCC 127 (14 Myr). This agrees with the suggestion that older clusters

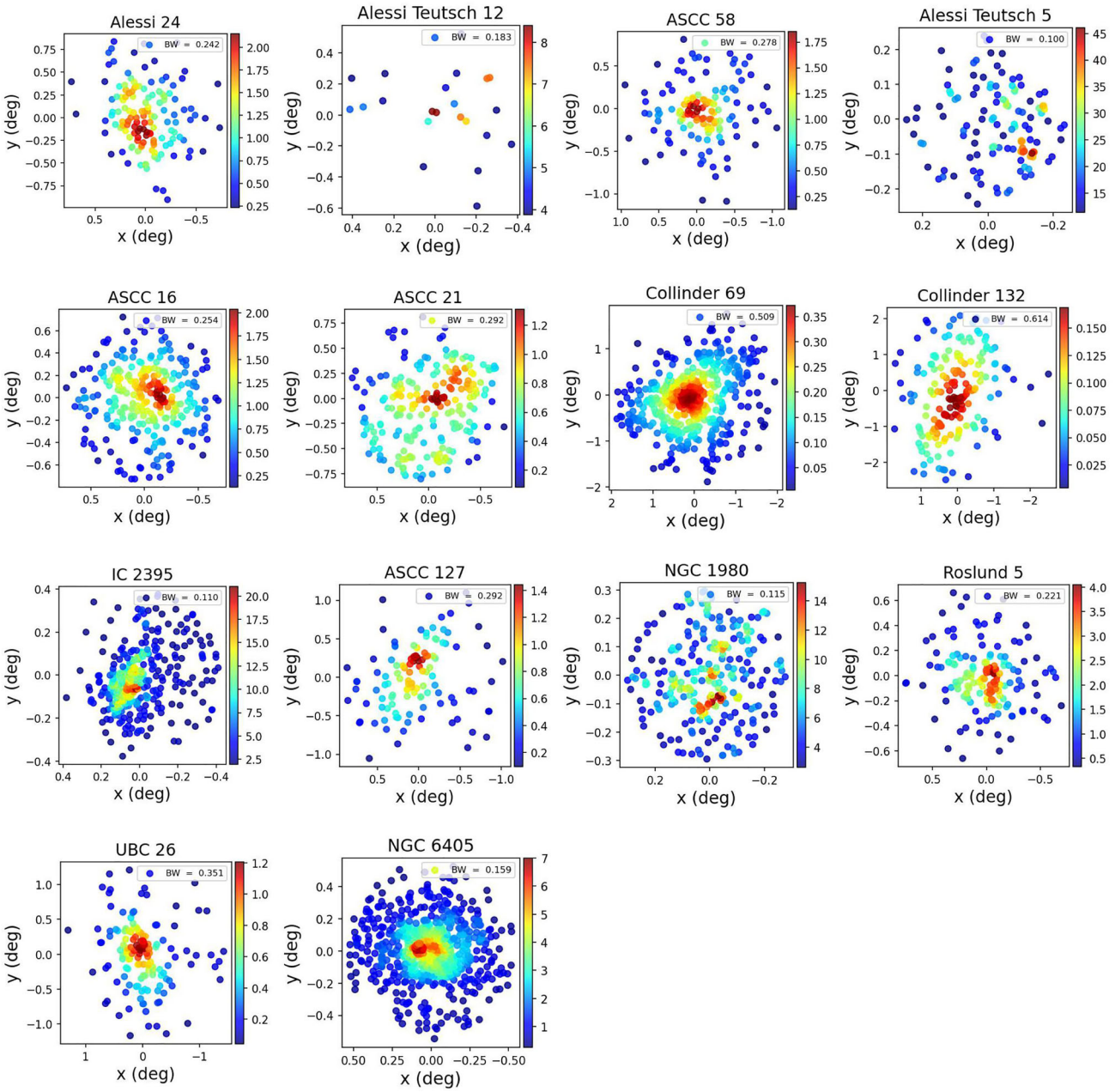

Figure 9. Kernel density diagrams for each cluster with the bandwidth (BW) used for plotting mentioned in the top right corner.

become more elliptical compared to younger ones, Zhai *et al.* (2017). Also, there are two clumps within Alessi 24. The difference in transverse velocity between the clumps is not found to be significant, suggesting that these clumps are not kinematically distinct in the sky plane. Radial velocity data is needed to estimate whether these clumps will merge or separate in the future. We also note some sub-structures in the full age range of clusters studied here. The spatial sub-structures found in clusters might indicate that clusters retain these for at least up to about 100 Myr.

3.8 *Binary clusters*

The fraction of binary clusters in the Milky Way Galaxy is 8% to 20% (Subramaniam *et al.* 1995; de La Fuente Marcos & de La Fuente Marcos 2009; Soubiran *et al.* 2018). ASCC 16 and ASCC 21 have been previously identified as a binary cluster by Soubiran *et al.* (2018). They have a similar age, $\log(\text{age}) = 7.157^{+0.005}_{-0.020}$, $7.021^{+0.011}_{-0.001}$, respectively, and similar metallicity, $[\text{M/H}] = -0.104^{+0.010}_{-0.007}$, $-0.107^{+0.016}_{-0.001}$, respectively. They have a transverse velocity difference of 0.39 km s^{-1}

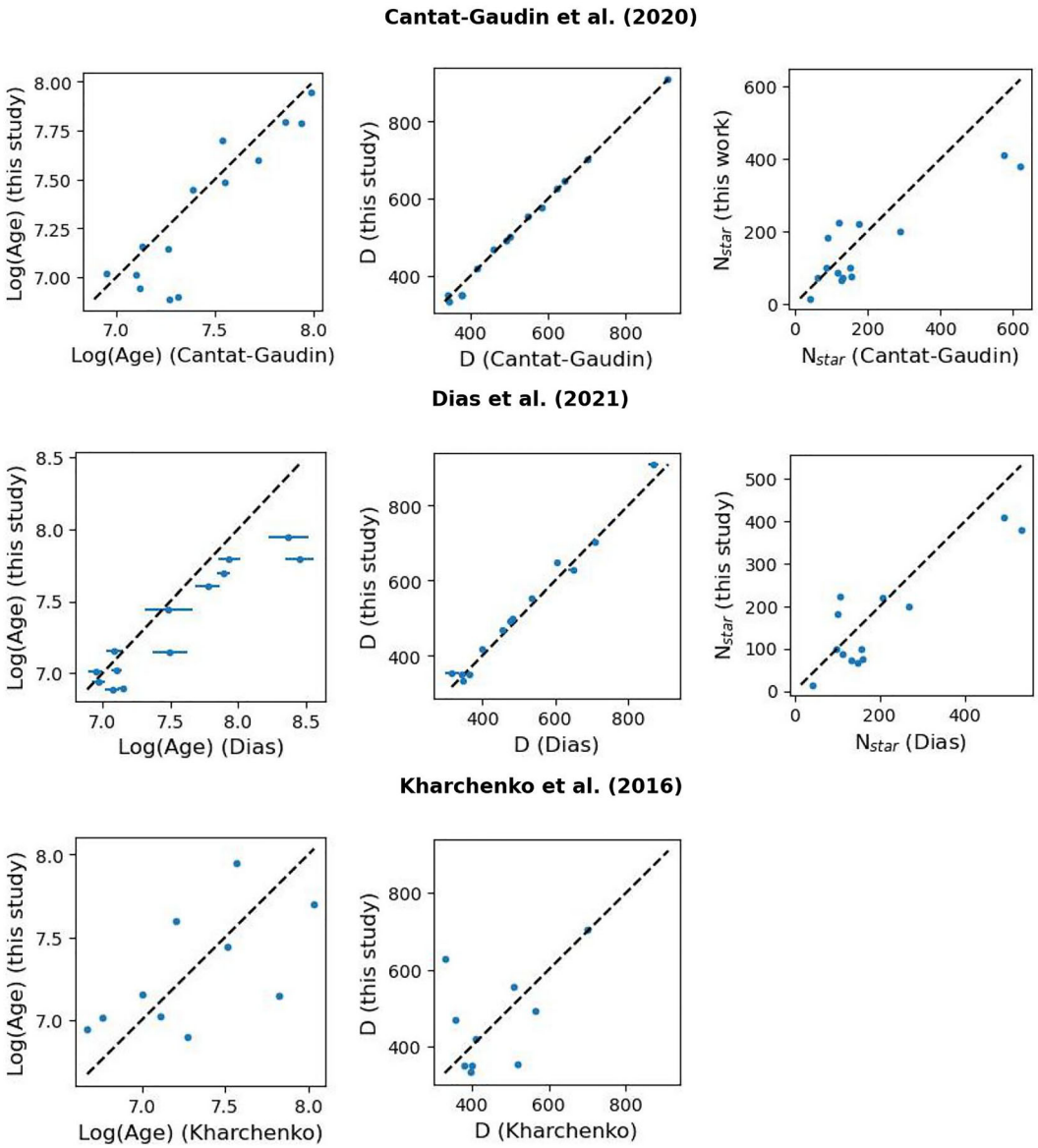

Figure A1. Comparison of cluster parameters with previous studies, such as Cantat-Gaudin *et al.* (2020), Kharchenko *et al.* (2016) and Dias *et al.* (2021).

and a space velocity difference of 1.02 km s^{-1}. Furthermore, their separation of 43.32 pc further suggests that these two clusters might have originated from the same molecular cloud around the same time.

4. Conclusions and summary

In this study, we present the kinematic and structural properties of 14 clusters using *Gaia* DR3 to link them to the details of internal dynamics and imprints of star formation in young clusters. The summary and conclusions of this study are given below:

- GMM method was used to find the membership information of the OCs. The clusters chosen are young (<100 Myr) and within a distance of 1 kpc, to study the internal kinematics as a function of mass within the clusters. The cluster parameters, such as age, distance, metallicity, and extinction, were estimated by fitting PARSEC isochrones to the CMDs, using a combination of a least-square minimization and MCMC technique. The code is automated to apply to a larger sample of clusters in the future.
- The clusters are found to be located between 350 and 910 pc, with an age ranging from 7.7 to 88 Myr, and near solar metallicity. The number of

Table A1. Cluster parameters obtained from literature survey Cantat-Gaudin *et al.* (2020). Columns 2 and 3 represent the coordinates of the corresponding cluster, RA and Dec, respectively. Columns 4 and 5 represent the PM along RA and Dec, respectively. *D* is the distance to the cluster, r50 is the radius containing half of the cluster members, Rmax is the r50×2 in arcminutes, and the last column represents the $\log_{10}$(age).

Cluster name	RA* (deg)	Dec* (deg)	pmra* (mas yr^{-1})	pmdec* (mas yr^{-1})	*D** (kpc)	r50* (deg)	Rmax (arcmin)	r50×2 (deg)	$\log_{10}$(age)*
Alessi 24	260.764	−62.693	−0.488	−8.999	0.502	0.466	55.92	0.932	7.86
Alessi Teutsch 12	255.421	−58.981	−2.134	−8.952	0.641	0.489	58.68	0.978	7.94
ASCC 58	153.657	−55.001	−13.276	2.786	0.491	0.592	71.04	1.184	7.72
Alessi Teutsch 5	332.218	61.103	−1.895	−3.207	0.907	0.125	15	0.25	7.27
ASCC 16	81.198	1.655	1.355	−0.015	0.344	0.376	45.12	0.752	7.13
ASCC 21	82.179	3.527	1.404	−0.632	0.341	0.41	49.2	0.82	6.95
Collinder 69	83.792	9.813	1.194	−2.118	0.416	0.989	118.68	1.978	7.1
Collinder 132	108.485	−30.758	−4.14	3.732	0.624	1.33	159.6	2.66	7.39
IC 2395	130.531	−48.09	−4.464	3.293	0.702	0.209	25.08	0.418	7.31
ASCC 127	347.205	+64.974	7.474	−1.745	0.376	0.627	75.24	1.254	7.26
NGC 1980	83.81	−5.924	1.215	0.54	0.377	0.151	18.12	0.302	7.12
Roslund 5	302.641	+33.751	1.981	−1.164	0.546	0.378	45.36	0.756	7.99
UBC 26	285.37	+22.020	2.049	−5.176	0.582	0.717	86.04	1.434	7.55
NGC 6405	265.069	−32.242	−1.306	−5.847	0.459	0.275	33	0.55	7.54

Note: *Obtained from Cantat-Gaudin catalogue.

member stars ranges from 22 to 641. Most of the low-mass (K- and M-type) stars in the cluster are in the pre-main-sequence (PMS) phase, whereas the high-mass stars are found to be in the main-sequence phase.

- 13 clusters are found to have a transverse velocity dispersion in the range of 0.28–0.70 km s^{-1}, with 10 clusters between 0.41 and 0.70 km s^{-1}. We suggest that this is the typical transverse velocity dispersion range in young clusters.
- Alessi Teutsch 12 has only 22 members, but has a low transverse velocity dispersion of $\sim 0.28 \pm 0.06$ km s^{-1}, suggesting that it is a poor open cluster. The largest transverse velocity dispersion 1.22 ± 0.11 km s^{-1} is found in Alessi Teutsch 5, with 118 members.
- The rich clusters in our sample, Collinder 69 (517 members), NGC 6405 (641 members), and IC 2395 (329 members) show a similar transverse velocity dispersion of ∼0.67–0.70 km s^{-1}.
- All clusters have stars in the B–M spectral type range. Alessi Teutsch 5, ASCC 16, ASCC 21, and NGC 1980 have stars more massive than 10 $M_\odot$. NGC 6405 has the largest number of B-type stars (19).
- Five clusters (Alessi 24, Collinder 132, IC 2395, NGC 1980, and ASCC 58) show increasing velocity dispersion from F- to M-type stars, a signature for dynamical relaxation for low-mass stars. The evidence of relaxation for low-mass stars in young clusters, such as IC 2395 (8 Myr) and NGC 1980 (9 Myr) are interesting.
- In the above clusters, we found that the B-A spectral types appear to have relatively higher or the same velocity dispersion as the FG type stars, suggesting the velocity-mass relation does not strictly hold. We are unsure about the cause of this phenomenon. This could be partially due to the low number of massive stars and/or the dynamic effects of binaries.
- This study, therefore, provides probably the first quantitative estimation of mass-dependent velocity dispersion as a pointer to dynamical relaxation in young clusters through transverse velocity dispersion estimates. This is an important pointer for numerical simulations of cluster dynamics, escape of low-mass stars, mass segregation, etc.
- We have found possible walkaway stars in 5 clusters (Alessi Teutsch 5, ASCC 16, ASCC 21, IC 2395, and NGC 6405). The highest relative velocity (3.3 km s^{-1}) is found for a 13 $M_\odot$ B-type star in Alessi Teutsch 5. The reason why we are not able to see stars with much higher velocities can possibly be due to the clustering algorithm

Table A2. Comparison of cluster parameters with previous studies, such as Cantat-Gaudin *et al.* (2020), Kharchenko *et al.* (2016) and Dias *et al.* (2021).

	N_{star}			D (pc)				$\log_{10}$(age) (dex)			
Cluster name	This study	Cantat-Gaudin	Dias	This study	Cantat-Gaudin	Kharchenko	Dias	This study	Cantat-Gaudin	Kharchenko	Dias
Alessi 24	135	157	159	$500.160^{+0.970}_{-0.811}$	502	...	482	$7.795^{+0.001}_{-0.002}$	7.86	...	8.457
Alessi Teutsch 12	22	41	43	$646.998^{+0.015}_{-0.020}$	641	...	605	$7.788^{+0.004}_{-0.007}$	7.94	...	7.935
ASCC 58	123	133	134	$490.998^{+0.100}_{-0.185}$	491	564	477	$7.601^{+0.005}_{-0.006}$	7.72	7.2	7.775
Alessi Teutsch 5	118	127	147	$910.018^{+0.039}_{-0.024}$	907	...	869	$6.886^{+0.001}_{-0.016}$	7.27	...	7.071
ASCC 16	280	175	207	$334.002^{+0.010}_{-0.009}$	344	397	348	$7.157^{+0.005}_{-0.020}$	7.13	7	7.088
ASCC 21	223	90	102	$350.006^{+0.010}_{-0.013}$	341	379	343	$7.021^{+0.011}_{-0.001}$	6.95	7.11	7.102
Collinder 69	517	620	532	$418.243^{+0.047}_{-0.069}$	416	411	400	$7.011^{+0.016}_{-0.057}$	7.1	6.76	6.946
Collinder 132	186	86	98	$628.000^{+0.031}_{-0.040}$	624	330	648	$7.445^{+0.031}_{-0.013}$	7.39	7.51	7.488
IC 2395	329	291	269	$704.001^{+0.006}_{-0.008}$	702	701	710	$6.897^{+0.005}_{-0.001}$	7.31	7.27	7.149
ASCC 127	113	117	113	$350.944^{+13.498}_{-3.142}$	376	400	365	$7.147^{+0.001}_{-0.000}$	7.26	7.82	7.496
NGC 1980	249	121	106	$351.984^{+6.310}_{-4.238}$	377	520	316	$6.940^{+0.008}_{-0.008}$	7.12	6.67	6.97
Roslund 5	151	151	158	$555.011^{+0.009}_{-0.017}$	546	508	536	$7.946^{+0.008}_{-0.003}$	7.99	7.57	8.373
UBC 26	140	64	...	$578.684^{+0.020}_{-0.012}$	582	...	...	$7.482^{+0.023}_{-0.028}$	7.55	...	...
NGC 6405	641	573	492	$468.003^{+0.020}_{-0.022}$	459	356	453	$7.697^{+0.009}_{-0.002}$	7.54	8.035	7.894

(GMM) we have used, which by default reduces the posterior probability of the stars with higher PM.

- We estimated the ratio of M/K type stars and compared them with the values expected from Kroupa and Salpeter IMF slopes. We note that the observed M/K ratio shows a trend with age, which might indicate the missing detection of M-type stars in younger clusters, resulting in a lower value of the ratio. On the other hand, the higher values found in 3 clusters (Alessi 24, ASCC 58, and Collinder 132, even with a higher transverse velocity dispersion for M-type stars) are likely to be real, but need more detailed study.
- The Spatial distribution of the members shows patterns, and we note clumpiness in a few clusters, including Alessi 24, which are kinematically indistinguishable. Elongated structures are seen in comparatively older clusters. The spatial substructures found in clusters might indicate that clusters retain these structures at least up to ∼90 Myr.
- We find that ASCC 16 (∼14 Myr) and ASCC 21 (∼10.5 Myr), suggested to be a binary cluster candidate, have a transverse velocity difference of 0.39 km s^{-1} and a space velocity difference of 1.02 km s^{-1}. Furthermore, their separation of 43.32 pc further suggests that these two clusters might have formed from the same molecular cloud, but are unlikely to be a binary.

Appendix: Literature survey

See Tables A1, A2, and Figure A1.

References

Allen C., Kinman T. 2004, in Revista Mexicana de Astronomia y Astrofisica Conference Series, Vol. 21, Revista Mexicana de Astronomia y Astrofisica Conference Series, Allen C., Scarfe C. (eds), p. 121

Bergond G., Leon S., Guibert J. 2001, A&A, 377, 462

Bhattacharya S., Rao K. K., Agarwal M., Balan S., Vaidya K. 2022, MNRAS, 517, 3525

Blaauw A. 1961, Bull. Astron. Inst. Netherlands, 15, 265

Bressan A., Marigo P., Girardi L. *et al*. 2012, MNRAS, 427, 127

Cantat-Gaudin T., Anders F., Castro-Ginard A. *et al*. 2020, A&A, 640, A1

Cardelli J. A., Clayton G. C., Mathis J. S. 1989, ApJ, 345, 245

Chen Y., Bressan A., Girardi L. *et al*. 2015, MNRAS, 452, 1068

Chen Y., Girardi L., Bressan A. *et al*. 2014, MNRAS, 444, 2525

Damian B., Jose J., Samal M. R. *et al*. 2021, MNRAS, 504, 2557

Dias W. S., Monteiro H., Moitinho A. *et al*. 2021, MNRAS, 504, 356

de Fuente Marcos R., de Fuente M. C. 2009, A&A, 500, L13

de Mink S. E., Brott I., Cantiello M. *et al*. 2012, in Astronomical Society of the Pacific Conference Series, Vol. 465, Proceedings of a Scientific Meeting in Honor of Anthony F. J. Moffat, Drissen L., Robert C., St-Louis N., Moffat A. F. J. (eds), p. 65

Eldridge J. J., Langer N., Tout C. A. 2011, MNRAS, 414, 3501

Foreman-Mackey D., Hogg D. W., Lang D., Goodman J. 2013, PASP, 125, 306

Fujii M. S., Portegies Z. S. 2011, Science, 334, 1380

Gaia Collaboration, Vallenari A., Brown A. G. A. *et al.* 2023, A&A, 674, A1

Gao X. 2018, AJ, 156, 121

Hogg D. W., Foreman-Mackey D. 2018, ApJS, 236, 11

Jadhav V. V., Pennock C. M., Subramaniam A., Sagar R., Nayak P. K. 2021, MNRAS, 503, 236

Kerr R., Kraus A. L., Rizzuto A. C. 2023, ApJ, 954, 134

Kharchenko N. V., Piskunov A. E., Schilbach E., Röser S., Scholz R. D. 2013, A&A, 558, A53

Kharchenko N. V., Piskunov A. E., Schilbach E., Röser S., Scholz R. D. 2016, A&A, 585, A101

Kroupa P. 2001, MNRAS, 322, 231

Kulesh M. V., Samirkhanova A. E., Carraro G. *et al*. 2024, AJ, 167, 212

Lada C. J., Lada E. A. 2003, ARA&A, 41, 57

Lada C. J., Margulis M., Dearborn D. 1984, ApJ, 285, 141

Leonard P. J. T. 1991, AJ, 101, 562

Luhman K. L., Esplin T. L., Loutrel N. P. 2016, ApJ, 827, 52

Margulis M., Lada C. J. 1984, in Star Formation Workshop, Edinburgh, Wolstencroft R. D. (ed), p. 41

McNamara B. J., Sekiguchi K. 1986, ApJ, 310, 613

O'Donnell J. E. 1994, ApJ, 422, 158

Park S.-M., Goodwin S. P., Kim S. S. 2017, in IAU Symposium, Vol. 316, Formation, Evolution, and Survival of Massive Star Clusters, Charbonnel C., Nota (eds), p. 261

Pecaut M. J., Mamajek E. E. 2013, ApJS, 208, 9

Perets H. B., Šubr L. 2012, ApJ, 751, 133

Poveda A., Ruiz J., Allen C. 1967, Boletin de los Observatorios Tonantzintla y Tacubaya, 4, 86

Renzo M., Zapartas E., Mink S. E. *et al*. 2019, A&A, 624, A66

Sagar R., Bhatt H. C. 1989, MNRAS, 236, 865

Salpeter E. E. 1955, ApJ, 121, 161

Soubiran C., Cantat-Gaudin T., Romero-Gómez M. *et al*. 2018, A&A, 619, A155
Suárez G., Downes J. J., Román-Zúñiga C. *et al*. 2019, MNRAS, 486, 1718
Subramaniam A., Gorti U., Sagar R., Bhatt H. C. 1995, A&A, 302, 86
Vasiliev E. 2019, MNRAS, 484, 2832
Wielen R. 1971, A&A, 13, 309
Zhai M., Abt H., Zhao G., Li C. 2017, AJ, 153, 57

Springer Nature or its licensor (e.g. a society or other partner) holds exclusive rights to this article under a publishing agreement with the author(s) or other rightsholder(s); author self-archiving of the accepted manuscript version of this article is solely governed by the terms of such publishing agreement and applicable law.